Int. J. Electron. Commun. (AEÜ) 154 (2022) 154337

Contents lists available at ScienceDirect

International Journal of Electronics and Communications

journal homepage: www.elsevier.com/locate/aeue

Short communication

A single-layer dual-band shielded HMSIW bandpass filter using single SIW cavity

Zhirui Zheng [a], Xiaoheng Tan [a,*], Daotong Li [a,b], Qiang Chen [b]

[a] School of Microelectronics and Communication Engineering, Chongqing University, Chongqing 400044, China
[b] Department of Communications Engineering, Tohoku University, Sendai 980-8579, Japan

ARTICLE INFO

Keywords:
Single-layer
Dual-band
Shielded HMSIW
Single SIW cavity

ABSTRACT

A single-layer dual-band shielded half mode substrate integrated waveguide (HMSIW) bandpass filter using single SIW cavity is proposed in this paper. A metallic wall is established along the longitudinal direction of the complete SIW cavity center and two gaps are etched near the metallic wall, two shielded HMSIW cavities are evolved from the single SIW cavity. These two shielded HMSIW cavities are coupled to each other by two interdigital structures. Moreover, TE_{101} and TE_{102} modes of both shielded cavities are utilized to form the lower and upper passband, respectively. Furthermore, complementary split-ring resonators (CSRRs) are used to easily adjust the frequency ratio of the two passbands, and a pair of open stubs are loaded on the feedlines to suppress the unwanted TE_{201} mode. The proposed filter is designed, analyzed, fabricated and measured. The tested results agree well with the simulated values. Two passbands with low insertion losses of 1.3 and 1.45 dB are centered at 3.03 and 3.92 GHz, respectively.

1. Introduction

Filters play an increasingly important role in multi-functional RF front-end of communication systems, which are in great demand in various application [1], especially for dual-band bandpass filters (DBBPFs) [2], which can effectively reduce the cost and the volume of systems. With the superior characteristics of low cost, coplanar structure, low insertion loss, high quality factor and high power-handing capability [3], substrate integrated waveguide (SIW) DBBPFs have been widely reported previously by adopting multiple SIW cavities [4–11], which results in larger size and more insertion loss for the directly cascaded form of multiple SIW cavities, such as [5] and [6]. Moreover, in [9] and [10], although double-/multi-layer substrates were utilized and multiple SIW cavities were stacked, they will increase the difficulty of processing and assembly. Therefore, there is a highly desire for the design of SIW DBBPFs with single SIW cavity and single layer substrate.

In order to realize miniaturization, half mode substrate integrated waveguide (HMSIW) DBBPFs are studied and reported [12–13]. Despite the DBBPFs based on HMSIW are achieved by loading E-shaped coupling slots [12], and complementary split-ring resonators (CSRRs) [13], the extra radiation loss is introduced due to the open boundary in conventional HMSIW structure, and the Q value will be reduced a lot compared with SIW structure. As a good solution, the partial mode filters with shielded structure are proposed, which can effectively decrease the radiation loss and improve Q value [14–15]. To the best of our knowledge, only very few DBBPFs utilized shielded HMSIW structure have been reported to date [16]. Nevertheless, the frequency skirt selectivity and out-of-band rejection in high frequencies of the third-order direct-coupled DBBPF reported in [16] need to be improved, and the relatively large size of 1.65 $\lambda_g \times 0.93\ \lambda_g$ is inevitable due to the cascaded of three shielded HMSIW cavities and one SIW cavity.

In this paper, a single-layer dual-band shielded HMSIW bandpass filter using single SIW cavity is proposed. Two main contributions of this paper are as follows

firstly, by building a metallic wall along the longitudinal direction of a SIW cavity center and etching a pair of gaps left and right of the metallic wall, two shielded HMSIW cavities can be evolved from a complete SIW cavity to realize miniaturization compared with cascaded SIW cavities. Moreover, the TE_{101} and TE_{102} modes in one shielded HMSIW cavity are coupled with the corresponding same modes in another shielded HMSIW cavity through two interdigital strictures, forming the lower and upper passbands with chebyshev-like response, respectively. The second, the CSRRs are employed on the cavities to

* Corresponding author.
E-mail address: txh@cqu.edu.cn (X. Tan).

https://doi.org/10.1016/j.aeue.2022.154337
Received 19 May 2022; Accepted 19 July 2022
Available online 22 July 2022
1434-8411/

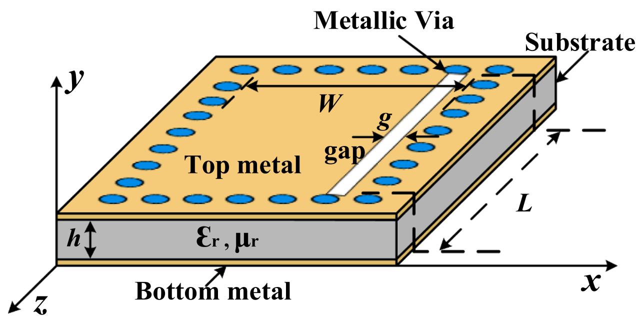

Fig. 1. Configuration of the shielded HMSIW cavity.

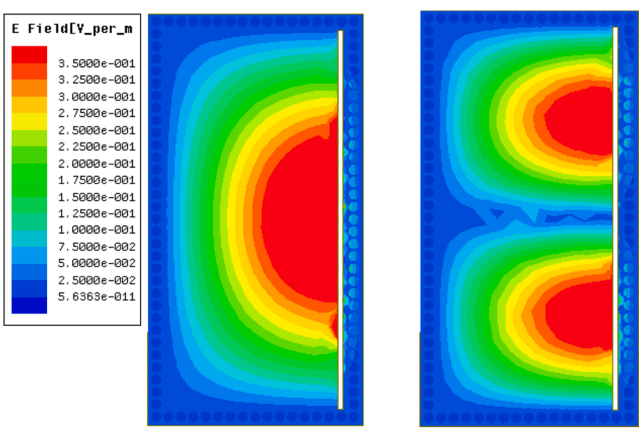

(a) (b)

Fig. 2. E-field distributions of the shielded HMSIW cavity. (a) TE_{101}. (b) TE_{102}.

easily adjust the frequency ratio of the two passbands. The inflexibility of directly changing the physical size of the SIW cavity to tune the frequency ratio is avoided, and the good shielding effect with relatively high unloaded quality factor is maintained. Open stubs and source-load coupling are used to reject the out-of-band TE_{201} mode and enhance roll-offs at sidebands, respectively, and a total of six transmission zeros (TZs) are generated in the stopband. This paper is arranged as follows. Section II describes the shielded HMSIW cavity analysis, the dual-band filter design and the analysis of the proposed filter. Section III presents the simulated and measured results, and the conclusions are drawn in Section IV.

2. Design and analysis

2.1. Shielded HMSIW cavity

Fig. 1 displays the configuration of the shielded HMSIW cavity with height of h, length of L and width of W, and g is the width of the gap, μ_r and ε_r are the relative permeability and relative permittivity of the substrate, respectively.

Compared with the complete SIW rectangular cavity, although the electric fields of the shielded HMSIW cavity can be cut in half, the modes also are expressed with the general forms [17].

$$f_{TE_{m0p}} = \frac{c}{2\sqrt{\mu_r \varepsilon_r}}\sqrt{\left(\frac{m}{W}\right)^2 + \left(\frac{p}{L}\right)^2} \tag{1}$$

where c is the light velocity in the free space, m and p are the mode indices along x- and z-axis directions, separately. In our design, TE_{101} and TE_{102} modes are employed, which can be expressed as.

$$f_{TE_{101}} = \frac{c}{2\sqrt{\mu_r \varepsilon_r}}\sqrt{\left(\frac{1}{W}\right)^2 + \left(\frac{1}{L}\right)^2} \tag{2}$$

$$f_{TE_{102}} = f_{TE_{101}}\sqrt{4 - \frac{3}{1 + (W/L)^2}} \tag{3}$$

and the electric filed (E-field) distributions of TE_{101} and TE_{102} modes are presented in Fig. 2.

According to formulation (2) and (3), the frequency ratio F_r between TE_{101} and TE_{102} modes can be obtained by.

$$F_r = f_{TE_{102}}/f_{TE_{101}} = \sqrt{4 - \frac{3}{1 + (W/L)^2}} \tag{4}$$

F_r and the resonant frequencies of TE_{101} and TE_{102} modes against g are depicted in Fig. 3(a) (It is obtained when $L = 40$ mm and $W = 38$ mm. The substrate is Rogers 4350 with the thickness of 0.508 mm, relative permeability of 3.48 and loss tangent of 0.004). It is clearly seen that g only has a slight influence on F_r and the frequency of TE_{101} and TE_{102} modes. So, the gap near the metallic vias generally retains the frequency characteristic of TE_{101} and TE_{102} modes in the HMSIW cavity under the condition of shielded structure. In addition, Fig. 3(b) displays the F_r varies with L and W. However, it's inflexible to obtain the required F_r through adjusting the physic size W and L of HMSIW cavity.

2.2. Dual-band filter design and analysis

In order to generate dual-band response using TE_{101} and TE_{102}

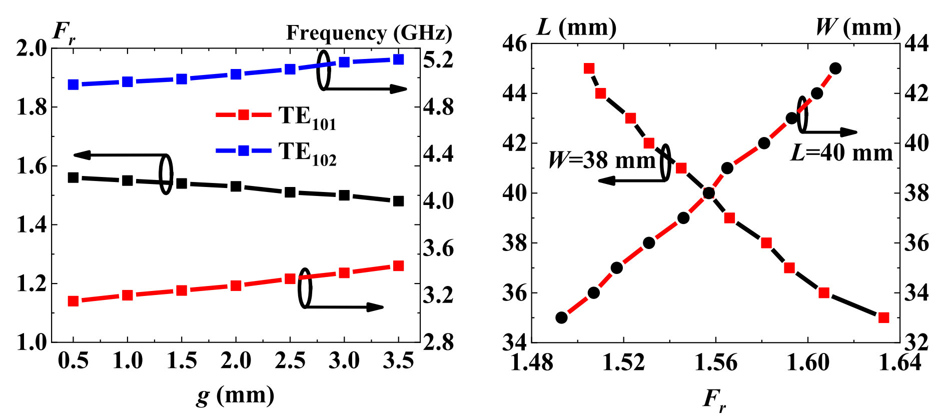

(a) (b)

Fig. 3. (a) F_r varies with g, and the frequency of TE_{101} and TE_{102} modes against g. (b) F_r varies with L (W = 38 mm) and W (L = 40 mm).

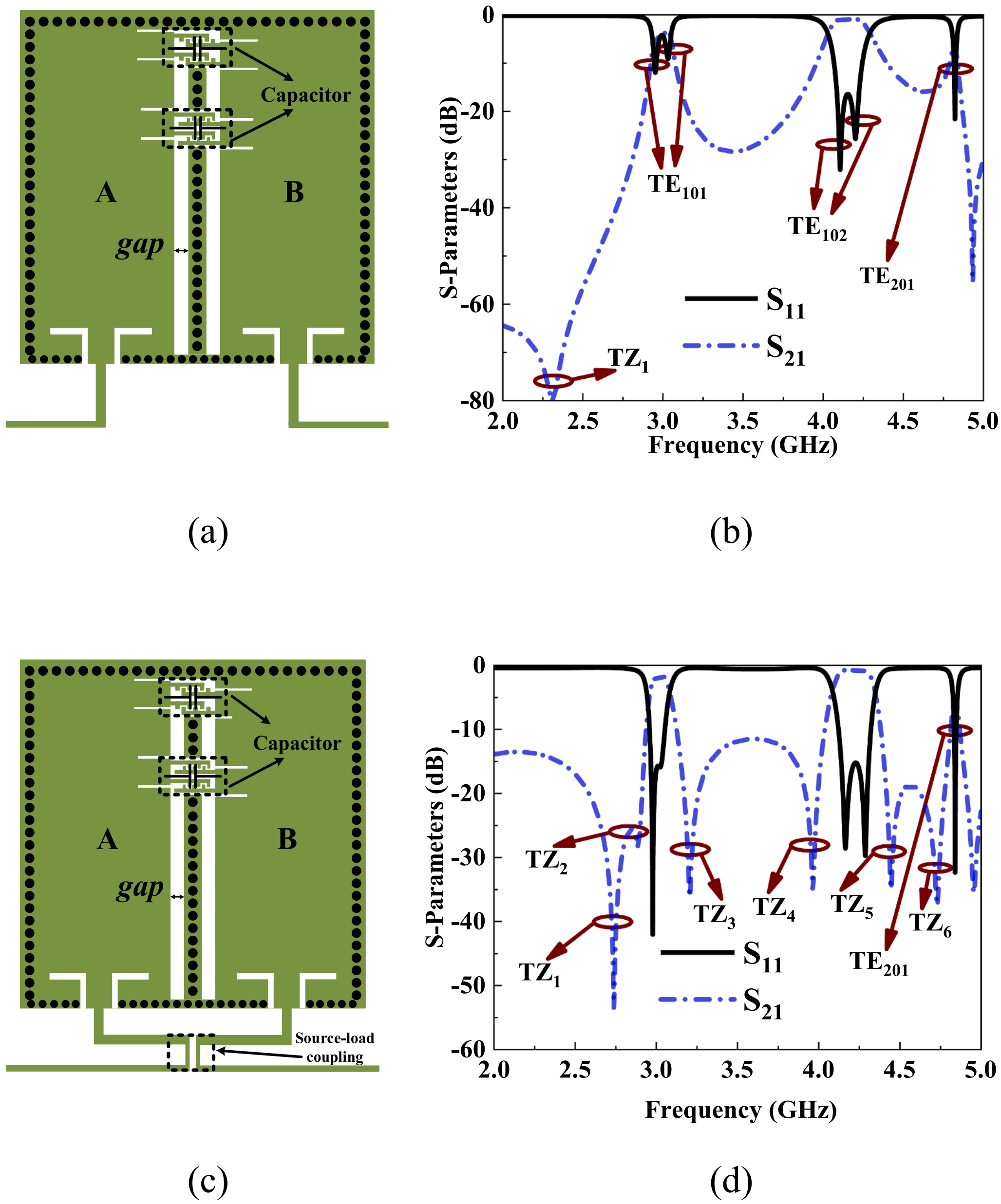

Fig. 4. (a) Filter I and (b) its S-Parameters. (c) Filter II and (d) its S-Parameters.

modes, a metallic wall functioned as an electric wall is established along the longitudinal direction of the single SIW cavity center and a pair of gaps are etched near the metallic wall. So, two shielded HMSIW cavities (A and B) can be obtained, which are coupled to each other through two interdigital structures equivalent to capacitors, and the configuration is shown in Fig. 4(a) and named as Filter I. Fig. 4(b) illustrates the simulated S_{11} and S_{21} of Filter I. Due to the mutual coupling between two shielded HMSIW cavities, two TE_{101} modes form the lower passband and two TE_{102} modes form the upper passband, and a chebyshev-like response with TZ_1 is acquired. However, the frequency skirt selectivity is relatively poor and needs to be enhanced. To further improve the selectivity, source-load coupling is adopted to establish Filter II, which is displayed in Fig. 4(c). Fig. 4(d) shows its simulated S-Parameters. As can be observed, five more TZs are introduced by source-load coupling and are located at both sides of the two passbands, and the selectivity and rejection are improved greatly. Although there is a TE_{201} mode located at 4.8 GHz which deteriorate the performance of upper stopband, by employing a couple of open stubs on the feed lines of Filter II, the TE_{201} mode at the upper stopband can be suppressed, as shown in Fig. 5.

By etching CSRR on the cavity, the surface current path can be changed, as a result, the resonance frequency can be turned by adjusting CSRR. Hence, when a pair of CSRRs are etched on the top layer of the cavities A and B of Filter II, the center frequency of the passbands can be changed accordingly, which is shown in Fig. 5. Therefore, the frequency ratio between the two operating bands can be controlled, which will be proved and discussed deeply in Subsection C. In addition, in order to investigate the effect of the etched CSRRs on the shielding performance of the shielded HMSIW cavity, Table 1 presents the unloaded quality

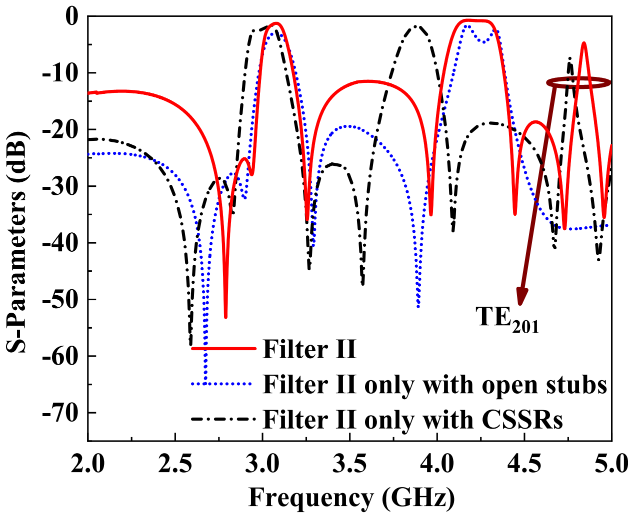

Fig. 5. Comparisons between Filter II, Filter II only with open stubs and Filter II only with CSRRs.

Table 1
Comparisons of unloaded quality factor Q for TE_{101} and TE_{102} modes of the three structures.

Structures Q Modes	Structure I	Structure II	Structure III
TE_{101} mode	410.98	405.84	389.33
TE_{102} mode	613.37	546.72	495.58

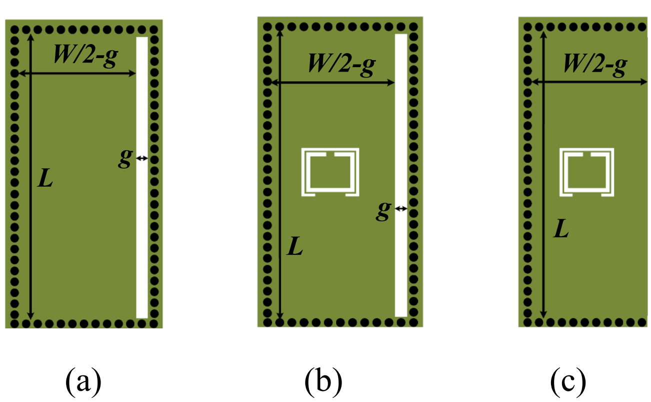

Fig. 6. Three types of structures. (a) Structure I. (b) Structure II. (c) Structure III.

factor Q for TE_{101} and TE_{102} modes of the three types of structures which are shown in Fig. 6. In Table 1, for the complete shielded structure, i.e. structure I, it has the highest Q values. Structure II which etched CSRRs reveals smaller Q values compared with structure I. While structure III with the fully open boundary displays lowest Q values. It can be concluded that although the CSRRs on the proposed configuration (Structure II) deteriorate the Q value to a certain degree, the proposed configuration still maintains the relatively high quality factor Q and has higher Q values than that of the conventional HMSIW structure with fully open boundary. Therefore, the shielded HMSIW cavity etched CSRRs still retains the good shielding effect.

Combined open stubs and CSRRs, the proposed filter is established as shown in Fig. 7. The presented filter is processed on the single substrate Rogers 4350 with the thickness of 0.508 mm, relative permeability of 3.48 and loss tangent of 0.004. To further reveal the effects of loading the open stubs and CSRRs at the same time, a comparison between the

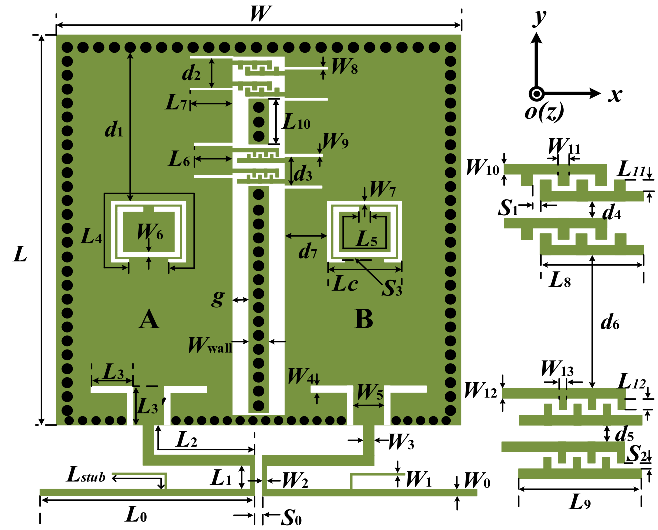

Fig. 7. Configuration of the proposed filter. ($L = 40$, $W = 38$, $L_0 = 20$, $L_1 = 5.5$, $L_2 = 12.81$, $L_3 = 4.67$, $L_3' = 5.05$, $L_4 = 29.2$, $L_5 = 22.6$, $L_6 = 2.77$, $L_7 = 3.19$, $L_8 = 4.3$, $L_9 = 5.1$, $L_{10} = 4.6$, $L_{11} = 0.19$, $L_{12} = 0.2$, $L_c = 0.2$, $L_{stub} = 8.7$, $W_0 = 1.25$, $W_1 = 0.12$, $W_2 = 0.97$, $W_3 = 1.9$, $W_4 = 0.37$, $W_5 = 2.8$, $W_6 = 0.5$, $W_7 = 0.3$, $W_8 = 0.2$, $W_9 = 0.3$, $W_{10} = 0.7$, $W_{11} = 0.5$, $W_{12} = 0.62$, $W_{13} = 0.19$, $S_0 = 0.6$, $S_1 = 0.18$, $S_2 = 0.29$, $S_3 = 0.2$, $d_1 = 15.2$, $d_2 = 3.4$, $d_3 = 3.34$, $d_4 = 0.4$, $d_5 = 0.49$, $d_6 = 5.3$, $d_7 = 2.9$, $g = 2$. Unit mm.).

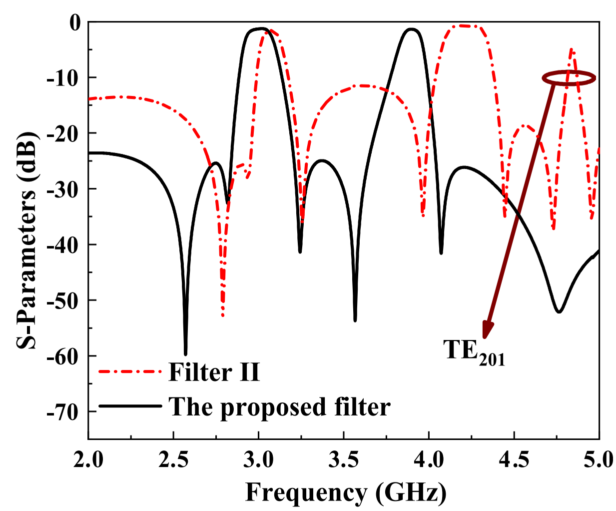

Fig. 8. Comparisons between the proposed filter and Filter II.

proposed filter and Filter II is presented in Fig. 8, which the smaller frequency ratio of two passbands and the suppression of unwanted TE_{201} mode can be observed, simultaneously.

2.3. Analysis of the proposed filter

Fig. 9(a) illustrates the coupling scheme of the proposed filter, where the red solid node denotes one shielded HMSIW cavity and the blue solid node denotes the other. A_1/B_1 and A_2/B_2 represent the TE_{101} and TE_{102} modes of cavity A/B, respectively. For the lower operating band, two TE_{101} modes coupled to each other through the electrical coupling (main coupling) provided by the interdigital structures, as well as the upper working band. Note that the jagged structures on the interdigital structures are used to increase the coupling strength between two shielded HMSIW cavities and improve impedance matching, which is shown in Fig. 9(b). Moreover, the resonance frequencies of the interdigital structures are much smaller than that of the two passbands, so the

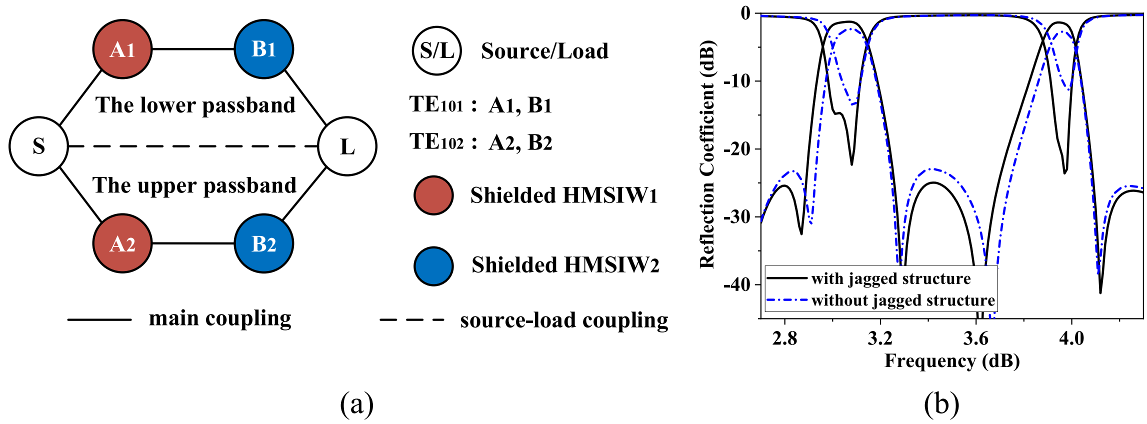

Fig. 9. (a) Coupling scheme of the proposed filter. (b) With and without the jagged structure on interdigital structures.

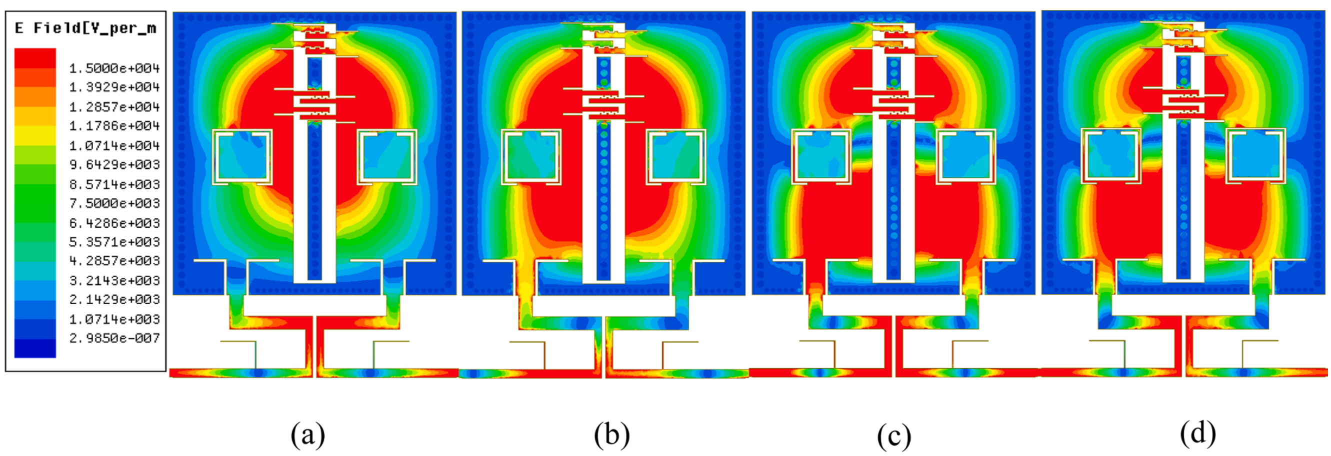

Fig. 10. The E-field distributions at the frequency of resonance nodes. (a) the first and (b) the second resonance node in the lower passband. (c) the first and (d) the second resonance node in the upper passband.

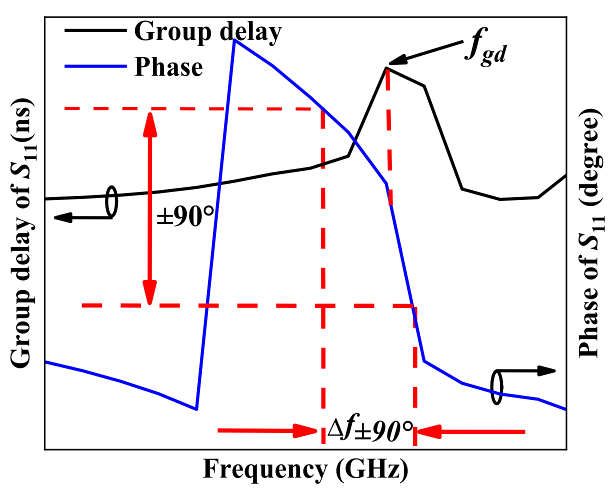

Fig. 11. The example of extracting external quality factor Q_e.

interdigital structures only functioned as couplers.

To further study the mechanism of the proposed filter, the E-field distribution at the frequency of each resonance node in passbands is illustrated in Fig. 10. It is obvious that the E-field distributions of the two resonance nodes in the lower passband are similar to that in Fig. 2(a), and the E-field distributions of the two resonance nodes in the upper passband are similar to that in Fig. 2(b). It further demonstrates that the lower passband consists of two TE_{101} modes, and the upper passband is composed of two TE_{102} modes. In addition, note that The upper interdigital structure is located where the E-field is weaker, while the lower interdigital structure is situated where the E-field is stronger. This arrangement is to fine-tune the coupling strength using the upper interdigitated structure, while the lower interdigitated structure is used to coarsely adjust the coupling strength.

The coupling coefficient K_{ij} ($j > i$) and external quality factor Q_e can be obtained by the following equations [18].

$$K_{ij} = \frac{f_j^2 - f_i^2}{f_j^2 + f_i^2} \tag{5}$$

$$Q_e = \frac{f_{gd}}{\Delta f_{\pm 90^\circ}} \tag{6}$$

where f_i and f_j ($j > i$) are the frequencies of resonance nodes, f_{gd} models the frequency at which the group delay of S_{11} reaches its maximum value and $\Delta f \pm 90^\circ$ is determined by the frequency at which the phase shifts $\pm 90^\circ$ relative to the absolute phase at f_{gd}, as shown in Fig. 11.

Fig. 12 present the variations of K(I) and K(II) versus key parameters L_9 and d_7, where K(I) and K(II) denote the coupling coefficients of two

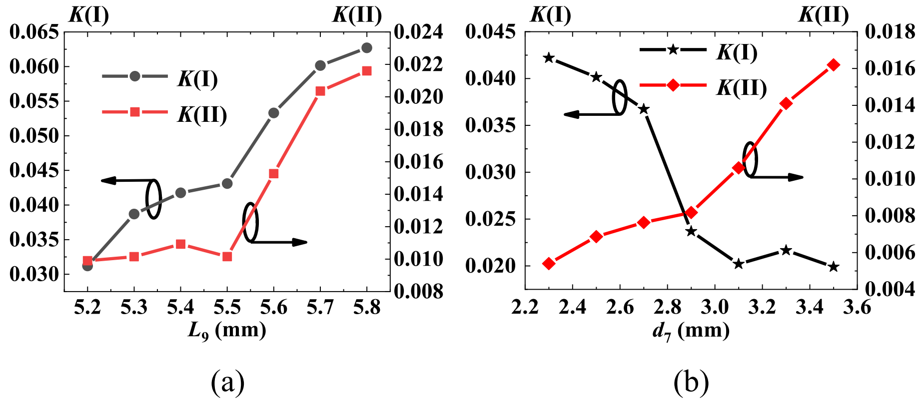

Fig. 12. Extracted coupling coefficients. (a) K(I) against varied L_9. (b) K(II) versus varied d_7.

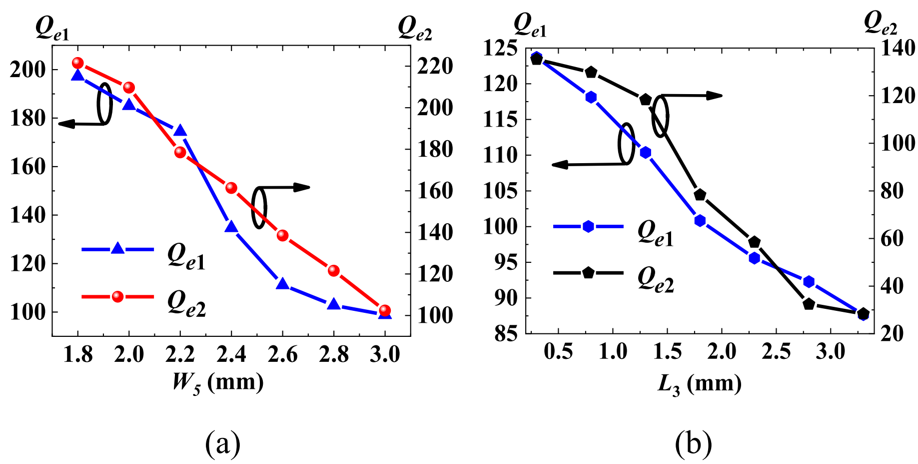

Fig. 13. Extracted external quality factors. (a) Q_{e1} against varied W_5. (b) Q_{e2} versus varied L_3.

TE_{101} and two TE_{102} modes, respectively. As the value of L_9 increases, K(I) and K(II) increase as a whole, which is shown in Fig. 12(a). In Fig. 12(b), when the value of d_7 is raised, K(I) will be reduced, while K(II) is increased. It reveals that the interdigital structures and the position of CSRRs can easily control the coupling coefficients. Fig. 13 illustrates the extracted external quality factors of the lower and upper passband, which are named as Q_{e1} and Q_{e2}, respectively. It can be observed that Q_{e1} and Q_{e2} can be affected readily by W_5 and L_3. Both Q_{e1} and Q_{e2} are changed monotonically at the same time while the value of W_5 and L_3 changes. In our design, the desired coupling coefficients are $K(\mathrm{I}) = 0.024$ and $K(\mathrm{II}) = 0.007$, and the required external quality factors are $Q_{e1} = 111.19$ and $Q_{e2} = 83.67$.

Furthermore, influences of the position d_1 and d_7 of CSRRs, the length L_c of CSRRs and the length L_9 of the interdigital structure are studied numerically, as depicted in Fig. 14. As can be seen in Fig. 14(a), with little effect on the lower passband, the upper passband can be easily controlled by tuning d_1. It should be noted that CSRRs are located in the middle of TE_{102} mode, which are shown in Fig. 10(c) and (d). When d_1 gets a smaller value, the red strong E-field in the upper part of TE_{102} mode can be further compressed by CSRRs, so that the upper passband is shifted to high frequencies. In Fig. 14(b), the frequency span between two passbands can be effectively adjusted by d_7, in which the frequency ratio is decreased as d_7 reduced. We can clearly observe from the surface current distributions presented in Fig. 15. In Fig. 15(a) and (b), for TE_{101} mode, the red strong current is mainly concentrated at the red arrows, when the value of d_7 decreases, the current path at the short arrow will be occupied by CSRRs, and then the total current path will be reduced, so the lower passband moves to high frequencies. In Fig. 15(c) and (d), for TE_{102} mode, the red strong current is mainly focus on the vicinity of the gap, when the value of d_7 reduced, the current path is cut off and the current flows around the CSRRs, so the total current path is increased and the upper passband is shifted to low frequencies. Thus, from Fig. 14(a) and (b), the controllable frequency ratio of two passbands can be obtained, as analyzed in Subsection B. In addition, the rejection and stopband bandwidth between two passbands also can be tuned through d_1 and d_7, as shown in Fig. 14(a) and (b). In Fig. 14(c), when L_c gets a bigger value, two passbands move to a lower frequency, simultaneously. It reveals the frequency adjustability of working passbands and a certain degree of miniaturization. In Fig. 14(d), the bandwidths of the two operational passbands can be adjusted by changing L_9, and the rejection levels are enhanced as L_9 increased. Therefore, based on the aforementioned analysis, the proposed filter has controllable frequency ratio, operating bands, bandwidth and rejection level.

3. Simulated and measured results

For demonstration, the proposed filter is optimized, fabricated and measured. The simulated/measured results of S-parameters of the proposed filter over the frequency range from 2 to 5 GHz are presented in Fig. 16(a). The lower and upper passbands are centered at 3.04/3.03

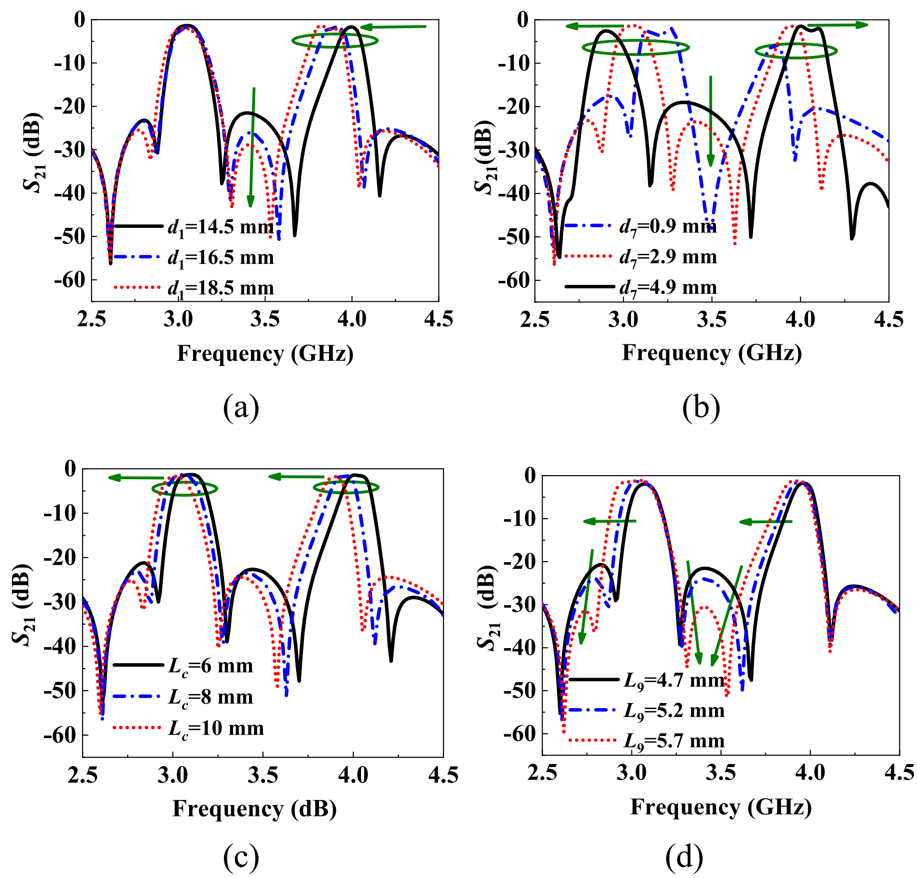

Fig. 14. Influences of (a) d_1, (b) d_7, (c) L_c and (d) L_9 on S_{21}.

GHz and 3.95/3.92 GHz, and the measured fractional bandwidth are 5.6% and 2.76%, respectively. For the two passbands, the return losses exceed 16/15 dB and 20/15 dB, respectively. The minimum in-band insertion losses are 1.0/1.3 dB and 1.1/1.45 dB, respectively. Six TZs situated at 2.62/2.61, 2.87/2.85, 3.29/3.27, 3.62/3.61, 4.12/4.09 and 4.84/4.63 GHz, separately, are generated in the stopband and located at the both sides of two passbands, which improve the frequency skirt selectivity and out-of-band suppression greatly. The maximum stopband rejection level reaches 59.8/55 dB. In addition, the measured frequency ratio between the two operating bands is 1.29. A good agreement between the tested and simulated results can be observed. The discrepancy is caused by the tolerance of the filter fabrication and the installation of Sub-Miniature Version A (SMA) connectors. Fig. 16(b) is the photo of the fabricated filter.

The comparisons between our design and some reported SIW DBBPFs are listed in Table 2. It can be concluded from the comparison table that the proposed filter has low in-band insertion losses, occupies a small size and only uses single SIW cavity and single layer substrate. Moreover, six deep TZs can be obtained by the proposed shielded configuration. These comparisons reveal the merits of the proposed filter and shows the proposed one is a good candidate for wireless communication application.

4. Conclusions

In this paper, a single-layer dual-band shielded HMSIW bandpass filter using single SIW cavity is proposed. The lower and upper passbands are composed of TE_{101} and TE_{102} modes of the two shielded HMSIW cavities, respectively. By etching CSRRs on shielded cavities, the frequency ratio of the two passbands can be easily adjusted to realize flexible adjustability. Moreover, the unwanted TE_{201} mode can be suppressed by the open stubs loaded on the feed lines. The proposed filter was fabricated and measured, the measured results agree well with simulated values. Two passbands were centered at 3.03 and 3.92 GHz, and six TZs are located at the both sides of the two passbands, which led to high selectivity and high rejection. The measured minimum insertion losses are 1.3 and 1.45 dB, which reached a low insertion loss level. In addition, the small size of 0.75 $\lambda_g \times$ 0.97 λ_g of the prototype filter is obtained. The proposed filter is a good candidate for dual-band communication application.

Declaration of Competing Interest

The authors declare that they have no known competing financial interests or personal relationships that could have appeared to influence the work reported in this paper.

Data availability

Data will be made available on request.

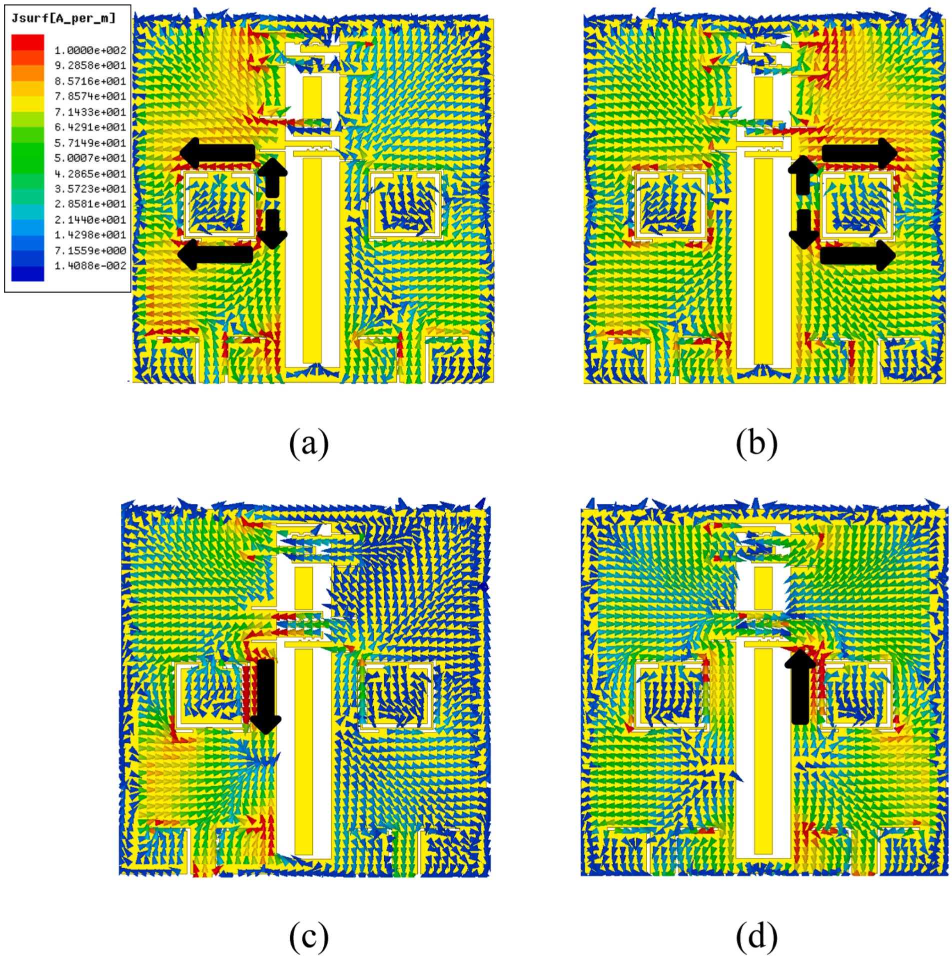

Fig. 15. The surface current distributions. (a) The first TE_{101} mode at 3.01 GHz and (b) the second TE_{101} mode at 3.08 GHz. (c) The first TE_{102} mode at 3.94 GHz and (d) the second TE_{102} mode at 3.97 GHz.

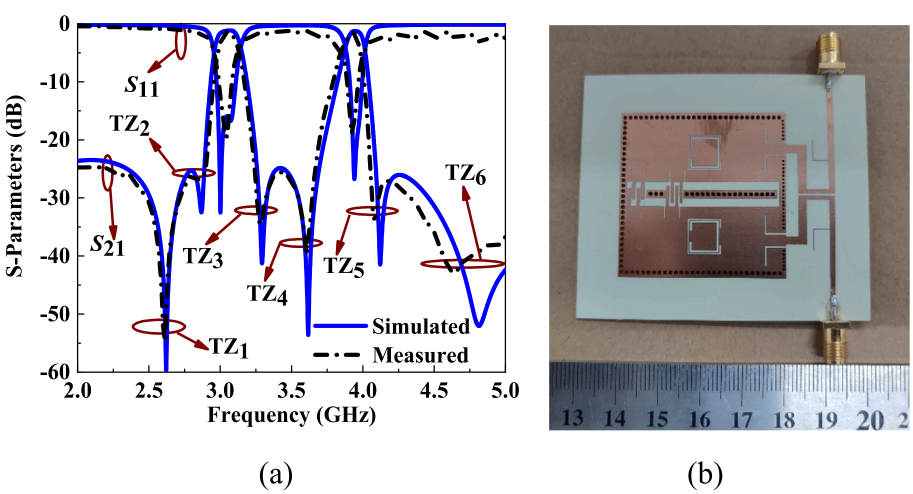

Fig. 16. (a) Simulated and measured S-Parameters of the proposed filter. (b)Photo of the fabricated filter.

Table 2
Comparisons between the proposed filter and reported SIW DBBPFs.

Ref.	TZ	FR*	SSIWC*	IL* (dB)	Size ($\lambda_g \times \lambda_g$)	SHMSIW*	f_0*
[4]	4	4/4	NO	1.74/ 2.21	1.13 × 1.02	NO	8.05/ 9.99
[6]	3	3/3	NO	2.26/ 3.07	1.31 × 1.66	NO	8.0/11.4
[7]	1	2/2	NO	1.8/1.4	0.71 × 1.59	NO	10.05/ 13.07
[8]	1	2/2	YES	1.9/ 1.65	1.26 × 1.26	NO	7.71/ 9.64
[9]	4	2/2	NO	0.68/ 0.61	1.15 × 1.15	NO	18.75/ 19.5
[10]	1	2/2	NO	2.25/ 1.92	$\pi \times 0.65^2$	NO	8.0/10.0
[11]	3	3/3	NO	2.86/ 3.37	3.32 × 1.16	NO	13.0/ 14.0
[12]	0	2/2	NO	2.0/1.8	0.39 × 0.69	NO	3.54/ 5.47
[13]	3	2/3	YES	0.76/ 1.4	0.92 × 0.53	NO	6.0/12.0
[16]	2	3/3	NO	1.65/ 2.25	1.65 × 0.93	YES	5.0/7.5
Prop.	**6**	**2/2**	**YES**	**1.3/ 1.45**	**0.75 × 0.97**	**YES**	**3.03/ 3.92**

FR* denotes filter order
SSIWC* represents single SIW cavity
IL* represents insertion loss
λ_g is the guided wavelength corresponding to the center frequency of the lower passband
SHMSIW* is shielded half mode SIW
f_0* denotes the center frequency of the filter.

Acknowledgment

This work was supported in part by the National Natural Science Foundation of China under Grant 61801059, in part by the National Natural Science Foundation of China under Grant U20A200726, in part by the Basic Research and Frontier Exploration Special of Chongqing Natural Science Foundation under Grant cstc2019jcyj-msxmX0350, in part by the FY2021 JSPS Postdoctoral Fellowship for Research in Japan under Grant P21053, and in part by the Grant-in-Aid for JSPS Research Fellow under Grant 21F21053.

References

[1] Cui Y, Xu K-D, Guo Y-J, Chen Q. Half-mode substrate integrated plasmonic waveguide for filter and diplexer designs. J Phys D Appl Phys 2022;55(12):125104. https://doi.org/10.1088/1361-6463/ac44bf.
[2] Kai-Da Xu, Shengpei Xia, Yannan Jiang, Yingjiang Guo, Yiqun Liu, Rui Wu, Jianlei Cui, and Qiang Chen. Compact millimeter-wave on-chip dual-band bandpass filter in 0.15-μm GaAs Technology. IEEE Journal of the Electron Devices Society. 2022 10 152-156.
[3] Yin Bo, Lin Z. A novel dual-band bandpass SIW filter loaded with modified dual-CSRRs and Z-shaped slot. AEU - Int J Electron Commun 2020;121:153261. https://doi.org/10.1016/j.aeue.2020.153261.
[4] Zhu Y, Dong Y. A compact dual-band quasi-elliptic filter based on hybrid SIW and microstrip technologies. IEEE Trans Circuits Syst II Express Briefs 2022;69(3):719–23.
[5] Zhou K, Zhou C-X, Wu W. Substrate-integrated waveguide dual-band filters with closely spaced passbands and flexibly allocated bandwidths. IEEE Trans Compon Packag Manuf Technol 2018;8(3):465–72.
[6] Xie H-W, Zhou K, Zhou C-X, Wu W. Compact SIW diplexers and dual-band bandpass filter with wide-stopband performances. IEEE Trans Circuits Syst II Express Briefs 2020;67(12):2933–7.
[7] Azad AR, Mohan A. Substrate integrated waveguide dual-band and wide-stopband bandpass filters. IEEE Microwave Wirel Compon Lett 2018;28(8):660–2.
[8] Azad AR, Mohan A. Single- and dual-band bandpass filters using a single perturbed SIW circular cavity. IEEE Microwave Wirel Compon Lett 2019;29(3):201–3.
[9] X. Zhou, G. Zhang, J. Zheng, W. Tang and J. Yang. SIW Filter With Adjustable Number of Passbands Using Assembled Multi-mode Resonant PCBs. IEEE Transactions on Circuits and Systems II Express Briefs. Early access, doi 10.1109/TCSII.2022.3157713.
[10] Han Y-K, Deng H-W, Zhu J-M, Xing S-B, Han W. Compact dual-band dual-mode SIW balanced BPF with intrinsic common-mode suppression. IEEE Microwave Wirel Compon Lett 2021;31(2):101–4.
[11] Xie H-W, Zhou K, Zhou C-X, Wu W. Compact wide-stopband SIW dual-band filter with closely spaced passbands. Electron Lett 2020;56:822–5.
[12] Iqbal A, Tiang JJ, Lee CK, Mallat NK, Wong SW. Dual-band half mode substrate integrated waveguide filter with independently tunable bands. IEEE Trans Circuits Syst II Express Briefs 2020;67(2):285–9.
[13] Fu W, Li Z, Liu P, Cheng J, Qiu X. Modeling and analysis of novel CSRRs-loaded dual-band bandpass SIW filters. IEEE Trans Circuits Syst II Express Briefs 2021;68(7):2352–6.
[14] Zheng Y, Zhu Y, Wang Z, Dong Y. Compact, wide stopband, shielded hybrid filter based on quarter-mode substrate integrated waveguide and microstrip line resonators. IEEE Microwave Wirel Compon Lett 2021;31(3):245–8.
[15] Wang X, Zong Z-Y, Wu W. Low phase noise oscillator employing miniaturized shielded-EMSIW resonators embedded with CSRRs structure. AEU-Int J Electron Commun 2022;151:154221. https://doi.org/10.1016/j.aeue.2022.154221.
[16] Zhou K, Zhou C, Wu W. Dual-mode characteristics of half-mode SIW rectangular cavity and applications to dual-band filters with widely separated passbands. IEEE Trans Microw Theory Tech 2018;66(11):4820–9.
[17] Liu Q, Zhang D, Tang M, Deng H, Zhou D. A class of box-like bandpass filters with wide stopband based on new dual-mode rectangular SIW cavities. IEEE Trans Microw Theory Tech 2021;69(1):101–10.
[18] Zhang H, Kang W, Wu W. Miniaturized dual-band SIW filters using E-shaped slotlines with controllable center frequencies. IEEE Microwave Wirel Compon Lett 2018;28(4):311–3.